Supplementary Material: Quantum Simulation of Spin-Boson Models with Structured Bath

Ke Sun,[1,2,*] Mingyu Kang,[1,2,†] Hanggai Nuomin,[3,‡] George Schwartz,[1,2]
David N. Beratan,[1,2,3,4] Kenneth R. Brown,[1,2,3,5] and Jungsang Kim[1,2,5]

[1]*Duke Quantum Center, Duke University, Durham, NC 27701, USA*
[2]*Department of Physics, Duke University, Durham, NC 27708, USA*
[3]*Department of Chemistry, Duke University, Durham, NC 27708, USA*
[4]*Department of Biochemistry, Duke University, Durham, NC 27710, USA*
[5]*Department of Electrical and Computer Engineering, Duke University, Durham, NC 27708, USA*

(Dated: October 27, 2024)

I. PARAMETER MAPPING

To illustrate how a trapped-ion simulator can simulate molecular energy transfer dynamics, we create a linear parameter mapping between the two systems. As a reference we define the unitless model with $\Delta = 1$. For the experiment in Fig. 3 of main text, the relationship between the unitless model and the molecular case is established by setting $\Delta = 500\,\mathrm{cm}^{-1}$ [1]. The other frequency parameters are then scaled linearly with Δ. The simulated evolution time T_{mol} is determined from the unitless model's evolution time T_{ul} by $\Delta_{\mathrm{mol}} T_{\mathrm{mol}} = \Delta_{\mathrm{ul}} T_{\mathrm{ul}}$, where the subscripts 'mol' and 'ul' represent molecular and unitless cases, respectively.

Similarly, the parameter $\kappa_{\mathrm{ul},l} T_{\mathrm{ul}} = \kappa_{\mathrm{ion},l} T_{\mathrm{ion},l}$ is used to determine the parameters for the trapped-ion simulator ('ion'), where $\kappa_{\mathrm{ion},l}$ and $T_{\mathrm{ion},l}$ denote the sideband Rabi frequency and the total operation time for driving the l-th mode, respectively. We choose $\kappa_{\mathrm{ion},l}$ as reference for calculating other parameters because the sideband transition frequency is relatively challenging to adjust precisely. Subsequently, $\nu_{\mathrm{ion},l}$ and $\Delta_{\mathrm{ion},l}$ for each mode are determined by $\Delta_{\mathrm{ul}} T_{\mathrm{ul}} = \sum_l \Delta_{\mathrm{ion},l} T_{\mathrm{ion},l}$ and $\nu_{\mathrm{ul},l} T_{\mathrm{ul}} = \nu_{\mathrm{ion},l} T_{\mathrm{ion},l}$. The resulting parameter mapping relationships for the 3-mode case are shown in Table I.

Model	Δ			κ			ν			Total time (T)		
Unitless	1.0			0.1	0.1	0.1	1.01	0.99	0.97	$12.8 \times 2\pi$		
Molecular (cm^{-1} or fs)	500			50	50	50	505	495	485	853.9		
Trapped ion ($2\pi\times$kHz or ms)	7.11	4.78	3.98	2.13	1.43	1.19	21.54	14.20	11.59	0.60	0.89	1.07

TABLE I. **Parameter mapping relations for the 3-mode experiment in Fig. 3 of main text.** For the trapped-ion case, the values for Δ, κ, ν, and T correspond to the spin detuning, sideband Rabi frequency, motion detuning, and total operation time, respectively, used in the operations driving each motional mode.

We perform similar calculations for the VAET case, as shown in Table II. The presence of ϵ requires single-qubit operations during the Trotter steps. The average phonon number $\bar{n}$ in the molecular context can be determined by $\bar{n} = 1/(\exp(\hbar\nu/k_B\mathcal{T}) - 1)$, where $\mathcal{T} = 300\mathrm{K}$ represents the room temperature.

Model	ϵ	Δ	κ	ν	Total time (T)	
Unitless	1.0	0.3	0.3	1.04	$12 \times 2\pi$	
Molecular (cm^{-1} or ps)	100	30	30	104	4.003	
Trapped ion ($2\pi\times$kHz or ms)	49.82	8	2.67	27.73	$T_{\mathrm{SQ}} = 0.24$	$T_{\mathrm{kick}} = 0.45$

TABLE II. **Parameter mapping relations for simulating VAET in Fig. 5(b) of main text.** For the trapped-ion case, the value for ϵ represents the carrier Rabi frequency during the single-qubit rotations, and the values for Δ, κ, ν correspond to the spin detuning, sideband Rabi frequency, and motion detuning, respectively, during the sideband-kick operations. Also, T_{SQ} and T_{kick} represent the total operation times for single-qubit rotations and sideband-kick operations, respectively.

* ke.sun@duke.edu
† mingyu.kang@duke.edu
‡ hanggai.nuomin@duke.edu

II. TOOLBOX FOR ACHIEVING HIGH-FIDELITY QUANTUM SIMULATION

A. Calibration

The calibration of a trapped-ion quantum simulator is crucial for achieving accurate and reliable results. The simulator relies on precise control and measurement of individual ions, and any misalignment can lead to errors in simulation. Proper calibration ensures that the simulator operates within its specified parameters. Additionally, calibration is necessary for maintaining consistency in simulations and enabling reproducibility of experimentally obtained results. In addition to standard calibrated parameters such as Raman transition frequency and motional frequencies, more specific and refined calibration parameters are considered for this quantum simulation circuit. This section mainly focuses on three calibration parameters that impact the fidelity of the simulation:

1. Spin phase difference between single qubit (SQ) and spin-dependent kick (SDK) operations
2. Light shift difference between SQ and SDK operations
3. Motional frequency re-calibration considering the light shift

1. Spin phase difference between SQ and SDK operations

In the trapped-ion experimental setup, we execute the SQ operation ($\hat{\sigma}_\alpha$) using a carrier Raman transition and perform the SDK operations ($\hat{\sigma}_\beta(\hat{b}+\hat{b}^\dagger)$) by simultaneously applying the blue- and red-sideband Raman transitions. Here, α in $\hat{\sigma}_\alpha \equiv \cos\alpha\hat{\sigma}_x + \sin\alpha\hat{\sigma}_y = e^{-i\alpha}\hat{\sigma}_+ + h.c.$ is the spin phase. In practice, the values of α and β differ due to various factors:

1. In the phase-sensitive geometry for Raman transitions, $\alpha - \beta = \pi/2$ [2, 3]
2. The laser power and phase gradients at the ion position introduces extra spin phase
3. Imperfect phase realization of the RFSoC system leads to a constant phase jump

To explain the first two factors, we consider the Taylor expansion of the phase-sensitive Raman transition Hamiltonian, where a single ion is considered for simplicity. Under a specific rotating frame, the interaction Hamiltonian can be expressed as [4]

$$\hat{H}_I = \frac{\Omega(x)}{2} e^{i(\Delta k x - \delta t - \Delta\phi)}\hat{\sigma}_+ + h.c., \tag{1}$$

where x is the ion's displacement from the equilibrium position along the direction of wavevector difference $\Delta\vec{k}$ between the two Raman beams, $\Delta k \equiv |\Delta\vec{k}|$, $\Omega(x)$ is the Rabi frequency of the phase-sensitive Raman transition at displacement x, δ is the frequency detuning from the carrier transition, and $\Delta\phi$ is the phase difference between the two Raman beams. Approximating this expression to the first order with respect to x, we obtain

$$\hat{H}_I \approx \left(\frac{\Omega(0)}{2} + (\frac{\Omega'(0)}{2} + i\Delta k\frac{\Omega(0)}{2})x\right) e^{i(-\delta t - \Delta\phi)}\hat{\sigma}_+ + h.c. \tag{2}$$

The position of ion can be quantized as

$$x = \sqrt{\frac{1}{2m\omega}}(\hat{b}e^{-i\omega t} + \hat{b}^\dagger e^{i\omega t}) \tag{3}$$

where ω denotes the motional frequency of this mode. Then, $\Delta k x = \eta(\hat{b}e^{-i\omega t} + \hat{b}^\dagger e^{i\omega t})$ where $\eta \equiv \Delta k\sqrt{\frac{1}{2m\omega}}$ represents the Lamb-Dicke parameter. Consequently, using the rotating-wave approximation (RWA), we can drive the on-resonance ($\delta = 0$) SQ operation described by the Hamiltonian

$$\hat{H}_{SQ} = \frac{\Omega(0)}{2} e^{-i\Delta\phi}\hat{\sigma}_+ + h.c. \tag{4}$$

Thus, the spin phase of the SQ operation is given by $\alpha = \Delta\phi$. When applying the SDK operation, we have

$$\begin{aligned}\hat{H}_{SDK} &= \hat{H}_I(\delta = -\omega) + \hat{H}_I(\delta = \omega) \\ &= (\frac{\Omega(0)'}{2}\frac{\eta}{\Delta k} + i\frac{\eta\Omega(0)}{2})e^{-i\Delta\phi}(\hat{b} + \hat{b}^\dagger)\hat{\sigma}_+ + h.c. \\ &= |A|(\hat{b} + \hat{b}^\dagger)(e^{i\gamma}e^{-i\Delta\phi}\hat{\sigma}_+ + h.c.),\end{aligned} \tag{5}$$

where $A = \frac{\Omega(0)'}{2}\frac{\eta}{\Delta k} + i\frac{\eta\Omega(0)}{2}$ and $\gamma = \mathrm{Arg}(A)$. When devoid of laser power and phase gradient considerations, i.e. $\Omega'(0) = 0$ and $\Omega(0)$ is real, the spin phase of the SDK operation is given by $\beta = \Delta\phi - \pi/2$, which agrees with $\alpha - \beta = \pi/2$ as stated above. However, with the inclusion of laser power gradient considerations, γ takes a nonzero value and introduces an additional spin phase component. Additionally, when considering the phase gradient of the laser wavepacket, $\Omega(x)$ is not necessarily a real number, introducing extra spin phase difference between the SQ and SDK operations.

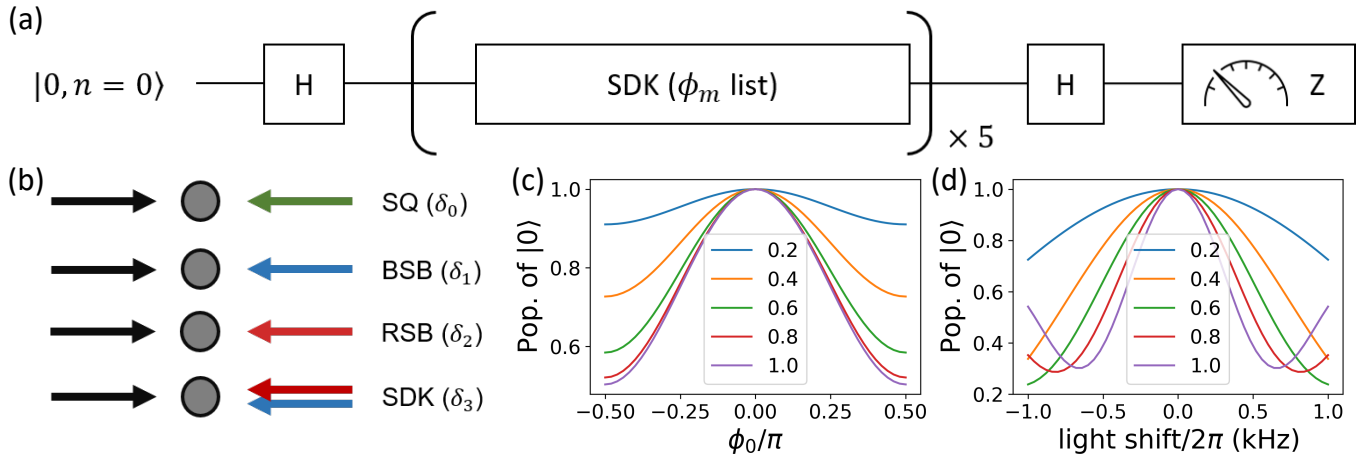

FIG. 1. **Calibration of light-shift differences.** **(a)** Illustration of pulse sequence used for calibrating the spin phase and light shift difference difference between the SQ and SDK operations. **(b)** Visual representation of the laser configurations for the SQ, blue/red sideband transition (BSB/RSB), and SDK operations. **(c) (d)** Expected probability of measuring the $|0\rangle$ state during the scanning of spin phase ϕ_0 and light shift of the SDK operations, respectively. For the different curves, duration of the SDK operation for each step is varied, where the legend labels indicate the duration divided by the sideband π-time.

In order to calibrate this spin phase difference between the SQ Hadamard gate and the SDK operation, the pulse sequence in Fig. 1a is employed, where the scanned spin phase of the SDK operation is denoted as ϕ_0. The ion is initialized in the ground state $|0, n = 0\rangle$. Subsequent to the Hadamard gate, the ion's spin becomes $|+\rangle = \frac{1}{\sqrt{2}}(|0\rangle + |1\rangle)$. Ideally, when ϕ_0 is zero, the $|+\rangle$ state is the eigenstate of the SDK operation's spin operator and remains unchanged throughout. Following this, the second Hadamard gate reverts the spin state back to $|0\rangle$, resulting in a population measurement of 1 for observing $|0\rangle$. In contrast, if $\phi_0 \neq 0$, the spin state will undergo changes during the SDK operation, leading to a deviation from a population measurement of 1, as shown in Fig. 1c. Thus, the spin phase difference between the SQ and SDK operations can be calibrated by finding the ϕ_0 value that gives the peak population of the $|0\rangle$ state. We note that the SDK operation is repeated five times where the list of motional phases is given by $[0, \pi, 0, \pi, 0]$ in order to prevent the ion from being excited to high motional states. Extending the SDK operation duration can amplify the accumulated errors and reduce the linewidth when scanning ϕ_0, thereby producing a more accurate calibration outcome.

2. *Light shift difference between SQ and SDK operations*

When performing the SQ and SDK operations on a trapped-ion quantum simulator, different laser settings are employed. Specifically, during the application of the SQ gate, an individual beam and a global beam with the carrier frequency are directed at the ion, as depicted in Fig. 1b. Conversely, for SDK operations, the global beam carries two tones with respective BSB and RSB transition frequencies. As a result, the light shift, which depends on the laser intensity, frequency, and polarization, varies between these two cases.

In order to calibrate this light shift difference, we propose a similar calibration method as depicted in Fig. 1a. We iteratively perform the pule sequence while varying the light shift frequency of the SDK operation. When there is a non-zero light shift difference between SQ and SDK, an additional spin phase accumulates during the SDK operation, resulting in a mixed state at the end. Consequently, the population of $|0\rangle$ deviates from 1, as shown in Fig. 1d. Similarly to above, extending the SDK operation duration can enhance the accuracy of the calibration.

3. *Motional frequency re-calibration considering the light shift*

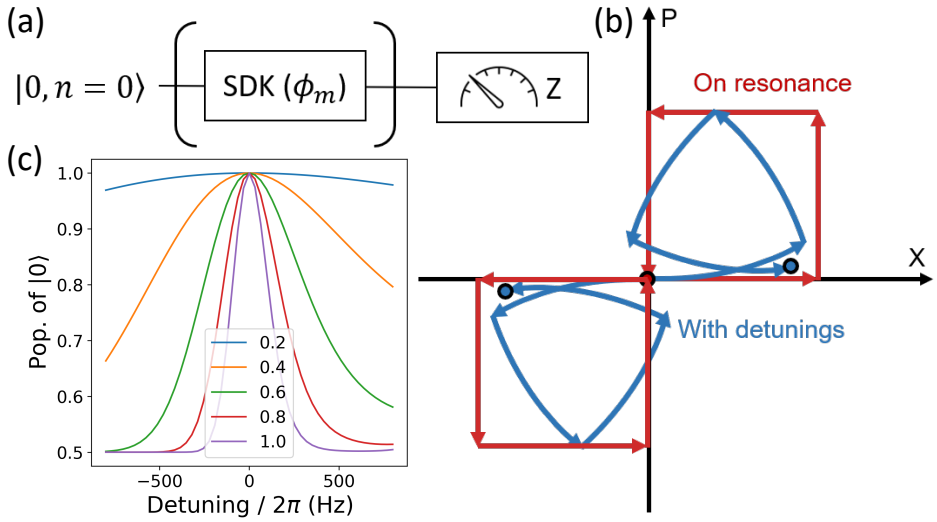

FIG. 2. **Motional frequency calibration.** **(a)** Illustration of pulse sequence used for calibrating the motional frequency. **(b)** Trajectory of ion in the phase space under this calibration scheme when the applied pulse is on resonance (red) or off resonance (blue). **(c)** Predictions of the measured population of the $|0\rangle$ state, where the motional detunings is scanned. The legend labels indicate the duration of each SDK operation divided by the sideband π-time.

Common techniques for calibrating the BSB and RSB frequencies involve either direct measurement of the transition's spectrum or indirect determination of the detunings via Ramsey interferometric fringes. As depicted in Fig. 1b, the calibration process for BSB and RSB frequencies typically utilizes a laser beam at a constant frequency, while scanning the frequency of the other beam around the relevant frequency. However, much like the situation described earlier, the light shifts experienced in these scenarios differ from those during the SDK operations, resulting in slight inaccuracies.

To address the potential inaccuracies in the calibration of motional frequencies, one straightforward approach is to employ the SDK operations for accurately determining the motional frequencies. This method is illustrated in Fig. 2a, beginning with the ion initialized in the ground state for both its spin and motion ($|n = 0\rangle$). Subsequently, four SDK pulses are applied at motional phases of 0, $\pi/2$, π, and $3\pi/2$. If the laser frequency perfectly matches the motional frequency, the ion's phase space trajectory will align with the red lines in Fig. 2b, ultimately returning to the original pure state $|0, n = 0\rangle$. However, if the laser frequency is detuned from the motional frequency, the ion will trace the blue trajectory, leading to a mixed state. When measuring the spin, the population of the $|0\rangle$ state will deviate from 1.

By scanning the detuning of the laser and measuring the population of the $|0\rangle$ state, we can identify the maximum point, which corresponds to the motional frequency we aim to calibrate (Fig. 2c). Moreover, increasing the SDK operation duration of each step reduces the linewidth of the scanned curve, improving the precision of the calibration. This method allows for precise calibration of the motional frequency, ensuring accurate and reliable simulations in the trapped ion quantum simulator.

B. Phase tracking

Once we have determined the frequencies and phases to be applied to the ion, it is essential to accurately implement the necessary control signals on the ion. Here we outline the procedures for controlling the laser phases to ensure

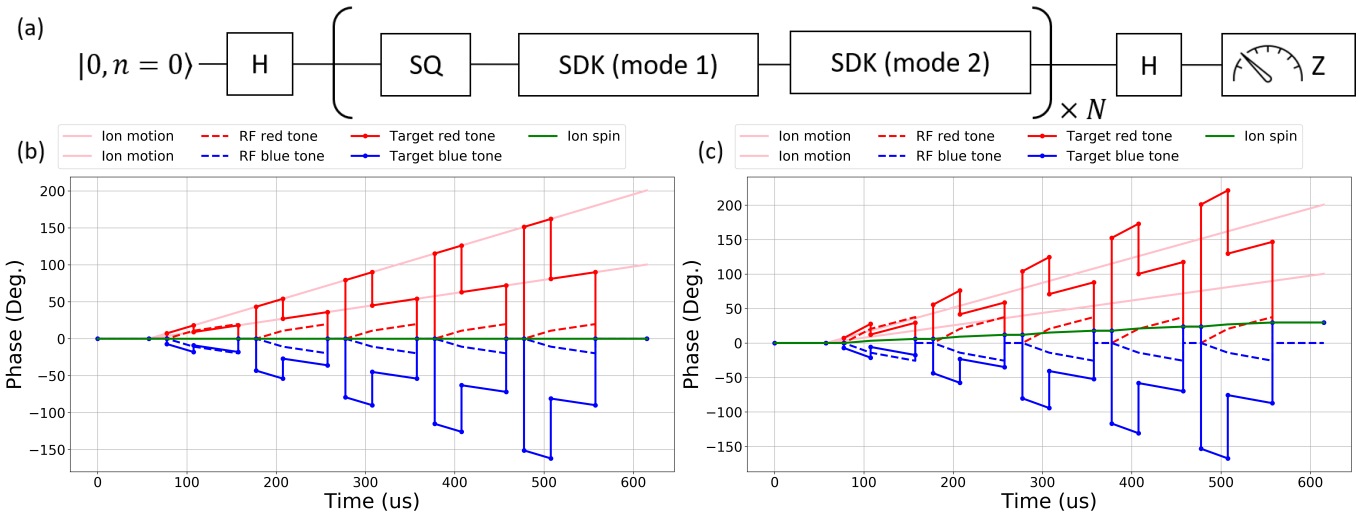

FIG. 3. **Demonstration of phase tracking.** **(a)** Pulse sequence used for showing the phases. **(b) (c)** Illustration of the evolution of different phases over time, including the spin and motion of the ion (ion spin/motion), the desired phases for implementing this pulse sequence (target red/blue tone), and the phases produced by the control software without applying additional phases (RF red/blue tone). Difference in light shifts between the SQ and SDK operations, as well as additional motional detunings, is assumed to be absent in (b) but present in (c).

synchronization with the ion phases. A simple pulse sequence shown in Fig. 3a is considered as an example that incorporates SQ rotations and SDK operations on two motional modes, where the number of Trotterization steps is set as $N = 5$. It is important to note that the parameter values used in this example are chosen for clear visualization and thus are not at scale.

Figure 3 displays the phases of the ion and the RFSoC control system. In this analysis, we utilize the frequency of the carrier transition ($|0\rangle$ to $|1\rangle$ transition) as the rotating frame. In practice, we set the repetition rate of the 355nm pulse laser to eliminate the light shift of the carrier transition. Thus, we assume the light shift of the carrier transition is zero. If not considering the light shift of the SDK operation, the spin phase of the ion remains constantly at zero in this frame, as indicated by the green line in Fig. 3b. Furthermore, regardless of the pulses applied to the ion, the motional modes oscillate at their respective motional frequencies. By setting the initial motional phase to zero at the start of the first SQ operation, the phase of the two motional modes of interest evolves as depicted by the two pink lines. To effectively monitor the ion's phase, we must align the phases of the lasers with the blue and red curves in Fig. 3b, which track the spin phase during the SQ operations and the blue and red motional phases during the SDK operations. Specifically, the target curves follow $\phi_{b,r} = \phi_s$ ($\phi_{b,r} = \phi_s \pm \phi_m$) for the SQ (SDK) operations. On the other hand, in the absence of additional phases applied to the RFSoC, the control system's phase follows the dashed curve if we sync the phase each time we apply an SQ operation. Consequently, we can determine the additional phase required to be added to the laser by subtracting the dashed curve from the solid curve.

We now take into account the difference in light shifts between the SQ and SDK operations. The green curve in Fig. 3c, which represents the ion spin's phase, exhibits a non-zero slope that is equivalent to the difference in light shifts, whenever a SDK operation is applied. Likewise, introducing additional detunings to the motional modes incurs the dashed curves to feature distinct slopes compared to the ion motion phase curves. Thus, the target phase curves need to be altered accordingly.

III. DAMPED VS. DEPHASED SPIN-OSCILLATOR MODEL

Two key ideas behind our experiment are (i) damped and dephased spin-oscillator models are described by the same 2-point correlation function (which determines the spectral density), and (ii) 2-point correlation function of the bath determines the spin dynamics up to leading order in the spin-bath coupling strength [5]. This enables our method of randomizing the control parameters to simulate the spin-boson model in the weak coupling regime.

A. Correlation functions of spin-oscillator models

We first introduce the 2-point correlation function of the bath. For simplicity, we consider a bath consisting of a single noisy oscillator; the correlation functions here can be straightforwardly generalized to a bath of multiple, or a continuum of, oscillators [6, 7]. The spin-oscillator composite state ρ follows the Lindblad master equation

$$\dot{\rho} = -i[\hat{H}_{SO}, \rho] + \sum_j (\hat{L}_j \rho \hat{L}_j^\dagger - \frac{1}{2}\{\hat{L}_j^\dagger \hat{L}_j, \rho\}), \tag{6}$$

where j is the index for different Lindblad operators $\hat{L}_j$ that act on the oscillator state only, and

$$\hat{H}_{SO} = \hat{H}_S + \hat{A}_S \otimes \hat{F}_O + \hat{H}_O. \tag{7}$$

Here, $\hat{A}_S = \hat{\sigma}_Z/2$, $\hat{F}_O = \kappa(\hat{b} + \hat{b}^\dagger)$, and $\hat{H}_O = \nu \hat{b}^\dagger \hat{b}$. We define the Lindblad generator $\mathcal{L}_O$ that describes the "free evolution" of the bath oscillator state ρ_O as

$$\mathcal{L}_O[\rho_O] = -i[\hat{H}_O, \rho_O] + \sum_j (\hat{L}_j \rho_O \hat{L}_j^\dagger - \frac{1}{2}\{\hat{L}_j^\dagger \hat{L}_j, \rho_O\}). \tag{8}$$

In this case, the 2-point correlation function of the bath between times t_0 and t_1 ($t_0 > t_1$) is defined as [6, 7]

$$C_O(t_0, t_1) = \mathrm{Tr}\left\{\hat{F}_O e^{\mathcal{L}_O(t_0 - t_1)}[\hat{F}_O e^{\mathcal{L}_O t_1}[\rho_O(0)]]\right\} \tag{9}$$

$$= \mathrm{Tr}\left\{\hat{F}_O e^{\mathcal{L}_O t}[\hat{F}_O \rho_O(0)]\right\} = C_O(t), \tag{10}$$

where $\rho_O(0)$ is the initial oscillator state and $t = t_0 - t_1$. From Eq. (9) to (10), we use the common assumption that the initial state is in equilibrium with dissipation, i.e., $\mathcal{L}_O[\rho_O(0)] = 0$. In the Heisenberg picture, Eq. (10) can be written as

$$C_O(t) = \mathrm{Tr}\left\{e^{\mathcal{L}_O^\dagger t}[\hat{F}_O]\hat{F}_O \rho_O(0)\right\}, \tag{11}$$

where $\mathcal{L}_O^\dagger$ is the *adjoint* Lindblad generator, such that [5]

$$\mathcal{L}_O^\dagger[\hat{F}_O] = i[\hat{H}_O, \hat{F}_O] + \sum_j (\hat{L}_j^\dagger \hat{F}_O \hat{L}_j - \frac{1}{2}\{\hat{L}_j^\dagger \hat{L}_j, \hat{F}_O\}). \tag{12}$$

The higher-order correlation functions can be defined as well. For example, the 4-point correlation function of the bath in the noisy spin-oscillator model can be written as

$$C_O^{(4)}(t_0, t_1, t_2, t_3) = \mathrm{Tr}\left\{\hat{F}_O e^{\mathcal{L}_O(t_0 - t_1)}[\hat{F}_O e^{\mathcal{L}_O(t_1 - t_2)}[\hat{F}_O e^{\mathcal{L}_O(t_2 - t_3)}[\hat{F}_O \rho_O(0)]]]\right\} \tag{13}$$

$$= \mathrm{Tr}\left\{e^{\mathcal{L}_O^\dagger(t_0 - t_1)}[e^{\mathcal{L}_O^\dagger(t_1 - t_2)}[e^{\mathcal{L}_O^\dagger(t_2 - t_3)}[\hat{F}_O]\hat{F}_O]\hat{F}_O]\hat{F}_O \rho_O(0)\right\} \tag{14}$$

where $t_0 > t_1 > t_2 > t_3$ and we again assume the initial-state equilibrium $\mathcal{L}_O[\rho_O(0)] = 0$.

Now we compare the correlation functions of the bath for the damped and dephased spin-oscillator models. First, damping is described by a pair of Lindblad operators $\hat{L}_1 = \sqrt{\Gamma(\bar{n}+1)}\hat{b}$ and $\hat{L}_2 = \sqrt{\Gamma \bar{n}}\hat{b}^\dagger$, where the bath oscillator's initial state $\rho_O(0)$ is given by the thermal state with average phonon number $\bar{n}$. The Lindblad generator $\mathcal{L}_O^{(\mathrm{damp})}$, obtained by substituting these $\hat{L}_j$'s into Eq. (8), satisfies $\mathcal{L}_O^{(\mathrm{damp})}[\rho_O(0)] = 0$ such that Eq. (10) is valid.

Next, dephasing is described by a single Lindblad operator $\hat{L}_1 = \sqrt{\Gamma}\hat{b}^\dagger \hat{b}$. The Lindblad generator $\mathcal{L}_O^{(\mathrm{deph})}$, obtained by substituting this $\hat{L}_j$ into Eq. (8), satisfies $\mathcal{L}_O^{(\mathrm{deph})}[\rho_O(0)] = 0$ for any diagonal state $\rho_O(0)$ such that Eq. (10) is valid.

Now we substitute $\hat{F}_O = \kappa(\hat{b} + \hat{b}^\dagger)$, which represents the linear spin-oscillator coupling, into Eq. (12). Interestingly, the Lindblad generators of the damped and dephased oscillators give the same result:

$$\mathcal{L}_O^{(\mathrm{damp})\dagger}[\hat{F}_O] = \mathcal{L}_O^{(\mathrm{deph})\dagger}[\hat{F}_O] = \kappa\left((-i\nu - \frac{\Gamma}{2})\hat{b} + (i\nu - \frac{\Gamma}{2})\hat{b}^\dagger\right). \tag{15}$$

Plugging this into Eq. (11), we obtain the bath's 2-point correlation function of both the damped and dephased spin-oscillator models, given by

$$C_O(t) = \kappa^2 e^{-\Gamma t/2}\left(\coth(\frac{\beta\nu}{2})\cos\nu t - i\sin\nu t\right), \tag{16}$$

where $\beta = \log(1+1/\bar{n})/\nu$ is the inverse of the temperature.

Note that the 2-point correlation function $C(t)$ and the spectral density $J(\omega)$ are closely related descriptions of the bath. In particular, for the spin-boson model, in which the bath is a continuum of oscillators, the two quantities are related by

$$C(t) = \int_0^\infty d\omega \frac{J(\omega)}{\pi}\left(\coth(\frac{\beta\omega}{2})\cos\omega t - i\sin\omega t\right). \tag{17}$$

For the damped spin-oscillator model, this relation is approximately true for the Lorentzian spectral density $J(\omega) = J_{\mathrm{Lo}}(\omega)$ in a reasonable regime of parameters ($\Gamma < \nu/2$, $\beta \ll 2\pi(\Gamma/2)^{-1}$) [8]. See Fig. 4a,b for the numerical agreement. Thus, in this paper, we conveniently use Eq. (17) to describe the spectral density of both the damped and dephased spin-oscillator models. As the 2-point correlation functions of the two models are the same as in Eq. (16), the same Lorentzian spectral density $J_{\mathrm{Lo}}(\omega)$ is assigned to the dephased spin-oscillator model. We leave a rigorous derivation of the dephased spin-oscillator model's spectral density, similarly to the work on the damped model [9], to future research.

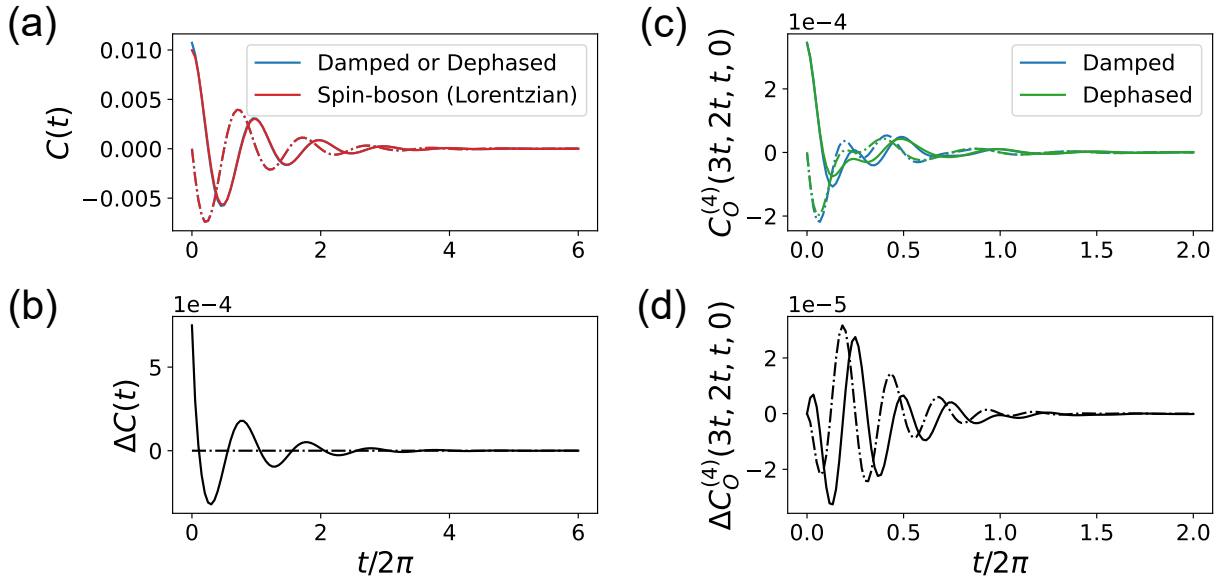

FIG. 4. **Correlation functions.** In all panels, $\nu = 1$, $\Gamma = 0.4$, $\kappa = 0.1$, and $\beta = 3.36$ ($\bar{n} = 0.036$). Solid (dot-dashed) curve is the real (imaginary) part. **(a)** 2-point correlation functions of the damped or dephased spin-oscillator model [see Eq. (16)] and the spin-boson model with Lorentzian spectral density $J(\omega) = J_{\mathrm{Lo}}(\omega)$ [see Eq. (17)], which match reasonably well. **(b)** Difference between the 2-point correlation functions in (a). **(c)** Examples of 4-point correlation functions of the damped and dephased spin-oscillator models, numerically calculated from Eq. (13). The results closely match Eqs. (18) and (19) obtained for $\bar{n} = 0$. **(d)** Difference between the 4-point correlation functions in (c).

While the 2-point correlation functions of the damped and dephased spin-oscillator models match, the 4-point correlation functions do not. This can be easily understood from the fact that $\mathcal{L}_O^{(\mathrm{damp})\dagger}[\hat{b}] = \mathcal{L}_O^{(\mathrm{deph})\dagger}[\hat{b}]$ and $\mathcal{L}_O^{(\mathrm{damp})\dagger}[\hat{b}^\dagger] = \mathcal{L}_O^{(\mathrm{deph})\dagger}[\hat{b}^\dagger]$ but $\mathcal{L}_O^{(\mathrm{damp})\dagger}[\hat{b}^\dagger\hat{b}] \neq \mathcal{L}_O^{(\mathrm{deph})\dagger}[\hat{b}^\dagger\hat{b}]$. For simplicity, we only show the 4-point correlation functions for the zero-temperature ($\bar{n} = 0$) case:

$$\text{Damped}: \quad C_O^{(4)}(t_0,t_1,t_2,t_3) = \kappa^4\left(e^{(-\Gamma/2-i\nu)(t_0-t_1+t_2-t_3)} + 2e^{(-\Gamma/2-i\nu)(t_0+t_1-t_2-t_3)}\right), \tag{18}$$

$$\text{Dephased}: \quad C_O^{(4)}(t_0,t_1,t_2,t_3) = \kappa^4\left(e^{(-\Gamma/2-i\nu)(t_0-t_1+t_2-t_3)} + 2e^{-\Gamma(t_1-t_2)}e^{(-\Gamma/2-i\nu)(t_0+t_1-t_2-t_3)}\right). \tag{19}$$

Examples of 4-point correlation functions are shown in Fig. 4c,d. Higher-order (6-point, 8-point, ...) correlation functions are also different between the two models.

Note that for the damped case, the 4-point correlation function can be expressed only using the 2-point correlation functions as

$$\text{Damped}: \quad C_O^{(4)}(t_0,t_1,t_2,t_3) = C_O(t_0,t_1)C_O(t_2,t_3) + C_O(t_0,t_2)C_O(t_1,t_3) + C_O(t_0,t_3)C_O(t_1,t_2), \tag{20}$$

which is a signature that the damping is Gaussian [10], i.e., the oscillator state is Gaussian at all times given a Gaussian initial state [6]. This can be understood from the fact that each term of $\mathcal{L}_O$ in Eq. (8) contains up to only two $\hat{b}$ or $\hat{b}^\dagger$. However, dephasing is not Gaussian, as terms in $\mathcal{L}_O$ contain at most four $\hat{b}$ or $\hat{b}^\dagger$. Thus, the 4-point correlation function cannot be expressed only using the 2-point correlation functions.

B. Spin dynamics and correlation functions

Following Ref. [5], the spin dynamics of the models here can be described in terms of the bath's correlation functions. We first transform the Hamiltonian $\hat{H}_{SO}$ into the interaction picture as

$$\hat{H}'_{SO}(t) = \hat{A}'_S(t) \otimes \hat{F}'_O(t), \tag{21}$$

where $\hat{A}'_S(t) := e^{i\hat{H}_S t}\hat{A}_S e^{-i\hat{H}_S t}$ and $\hat{F}'_O(t) := e^{\mathcal{L}_O^\dagger t}[\hat{F}_O]$. The spin-oscillator density matrix $\rho'(t)$ in the interaction picture evolves with respect to the generator $\mathcal{L}'(t)$ as

$$\dot{\rho}'(t) = \mathcal{L}'(t)[\rho'(t)] = -i[\hat{H}'_{SO}(t), \rho'(t)]. \tag{22}$$

Note that interaction picture is typically defined for the case where a static Hamiltonian, rather than a Lindblad generator such as $\mathcal{L}_O$, is rotated out. Thus, for mathematical rigor, the noisy spin-oscillator model first needs to be embedded into a tripartite spin-oscillator-environment system undergoing a corresponding unitary evolution, as in Lemma 1 of Ref. [6]. Then, the interaction picture is obtained by rotating out the Hamiltonian of the oscillator-environment subsystem.

To extract the spin dynamics, we use the time-convolutionless (TCL) projection operator method [5, 11]. We introduce the projection operator $\mathcal{P}$, defined as

$$\mathcal{P}\rho'(t) = \rho'_S(t) \otimes \rho_O(0), \tag{23}$$

where $\rho'_S(t) = \mathrm{Tr}_O\{\rho'(t)\}$, such that $\mathcal{P}\rho'(t)$ contains the information about the spin part of $\rho'(t)$. Then we obtain the TCL master equation for $\mathcal{P}\rho'(t)$ as

$$\frac{\partial}{\partial t}\mathcal{P}\rho'(t) = \sum_{n=1}^{\infty} \mathcal{K}_n(t)\mathcal{P}\rho'(t), \tag{24}$$

where $\mathcal{K}_n(t)$ is the n-th order TCL generator. The TCL generators up to fourth order are given by

$$\mathcal{K}_1(t) = \mathcal{K}_3(t) = 0, \tag{25}$$

$$\mathcal{K}_2(t) = \int_0^t dt_1 \mathcal{P}\mathcal{L}'(t)\mathcal{L}'(t_1)\mathcal{P}, \tag{26}$$

$$\begin{aligned}\mathcal{K}_4(t) = \int_0^t dt_1 \int_0^{t_1} dt_2 \int_0^{t_2} dt_3 \Big(&\mathcal{P}\mathcal{L}'(t)\mathcal{L}'(t_1)\mathcal{L}'(t_2)\mathcal{L}'(t_3)\mathcal{P} - \mathcal{P}\mathcal{L}'(t)\mathcal{L}'(t_1)\mathcal{P}\mathcal{L}'(t_2)\mathcal{L}'(t_3)\mathcal{P} \\ &- \mathcal{P}\mathcal{L}'(t)\mathcal{L}'(t_2)\mathcal{P}\mathcal{L}'(t_1)\mathcal{L}'(t_3)\mathcal{P} - \mathcal{P}\mathcal{L}'(t)\mathcal{L}'(t_3)\mathcal{P}\mathcal{L}'(t_1)\mathcal{L}'(t_2)\mathcal{P}\Big).\end{aligned} \tag{27}$$

In Eq. (27), the first term of the integrand starts and ends with $\mathcal{P}$, while the other three terms have another $\mathcal{P}$ multiplied in the middle. The odd-order TCL generators are zero because they involve odd number of $\hat{b}$ or $\hat{b}^\dagger$ applied to the diagonal state $\rho_O(0)$, followed by $\mathcal{P}$ which traces out the oscillator. Also note that for even n, $\mathcal{K}_n(t)$ is proportional to κ^n, as $\hat{H}'_{SO}(t) \propto \kappa$. Thus, the TCL master equation in Eq. (24) can be thought as a perturbation expansion with respect to the spin-oscillator coupling strength κ.

We first write the second-order term of Eq. (24) using the bath's 2-point correlation function $C_O(t,t_1)$. Here we define $\hat{0} \equiv \hat{A}'_S(t)$ and $\hat{1} \equiv \hat{A}'_S(t_1)$, using the notation of Ref. [5]. By straightforward algebra,

$$\begin{aligned}
\mathcal{K}_2(t)\rho'_S(t)\otimes\rho_O(0) &= -\int_0^t dt_1 \mathrm{Tr}_O\Big\{[\hat{H}'_{SO}(t),[\hat{H}'_{SO}(t_1),\rho'_S(t)\otimes\rho_O(0)]]\Big\}\otimes\rho_O(0) \\
&= -\int_0^t dt_1 \mathrm{Tr}_O\Big\{\hat{0}\hat{1}\rho'_S(t)\otimes\hat{F}'_O(t)\hat{F}'_O(t_1)\rho_O(0) + \rho'_S(t)\hat{1}\hat{0}\otimes\rho_O(0)\hat{F}'_O(t_1)\hat{F}'_O(t) \\
&\qquad\qquad - \hat{0}\rho'_S(t)\hat{1}\otimes\hat{F}'_O(t)\rho_O(0)\hat{F}'_O(t_1) - \hat{1}\rho'_S(t)\hat{0}\otimes\hat{F}'_O(t_1)\rho_O(0)\hat{F}'_O(t)\Big\}\otimes\rho_O(0) \\
&= -\int_0^t dt_1 \Big(C_O(t,t_1)(\hat{0}\hat{1}\rho'_S(t) - \hat{1}\rho'_S(t)\hat{0}) - C^*_O(t,t_1)(\hat{0}\rho'_S(t)\hat{1} - \rho'_S(t)\hat{1}\hat{0})\Big)\otimes\rho_O(0), \qquad (28)
\end{aligned}$$

where * denotes complex conjugate and we use Eq. (9) to go from second to third line. Thus, separating out $\rho_O(0)$ from both sides, this gives the $\mathcal{O}(\kappa^2)$ term of the time evolution of the spin.

The fourth-order term of Eq. (24) can be written in terms of the bath's 4-point correlation function in Eq. (13). Using the notation $\hat{2} \equiv \hat{A}'_S(t_2)$ and $\hat{3} \equiv \hat{A}'_S(t_3)$, similar algebra yields

$$\begin{aligned}
\mathcal{K}_4(t)\rho'_S(t)\otimes\rho_O(0) = \int_0^t dt_1\int_0^{t_1} dt_2\int_0^{t_2} dt_3 \\
\Big(C^{(4)}_O(t,t_1,t_2,t_3)(\hat{0}\hat{1}\hat{2}\hat{3}\rho'_S(t) - \hat{1}\hat{2}\hat{3}\rho'_S(t)\hat{0}) - C^{(4)*}_O(t,t_1,t_2,t_3)(\hat{0}\rho'_S(t)\hat{3}\hat{2}\hat{1} - \rho'_S(t)\hat{3}\hat{2}\hat{1}\hat{0}) \\
- C^{(4)}_O(t_2,t,t_1,t_3)(\hat{0}\hat{1}\hat{3}\rho'_S(t)\hat{2} - \hat{1}\hat{3}\rho'_S(t)\hat{2}\hat{0}) + C^{(4)*}_O(t_2,t,t_1,t_3)(\hat{0}\hat{2}\rho'_S(t)\hat{3}\hat{1} - \hat{2}\rho'_S(t)\hat{3}\hat{1}\hat{0}) \\
- C^{(4)}_O(t_1,t,t_2,t_3)(\hat{0}\hat{2}\hat{3}\rho'_S(t)\hat{1} - \hat{2}\hat{3}\rho'_S(t)\hat{1}\hat{0}) + C^{(4)*}_O(t_1,t,t_2,t_3)(\hat{0}\hat{1}\rho'_S(t)\hat{3}\hat{2} - \hat{1}\rho'_S(t)\hat{3}\hat{2}\hat{0}) \\
+ C^{(4)}_O(t_2,t_1,t,t_3)(\hat{0}\hat{3}\rho'_S(t)\hat{2}\hat{1} - \hat{3}\rho'_S(t)\hat{2}\hat{1}\hat{0}) - C^{(4)*}_O(t_2,t_1,t,t_3)(\hat{0}\hat{1}\hat{2}\rho'_S(t)\hat{3} - \hat{1}\hat{2}\rho'_S(t)\hat{3}\hat{0})\Big)\otimes\rho_O(0). \qquad (29)
\end{aligned}$$

Again, separating out $\rho_O(0)$ from both sides, this gives the $\mathcal{O}(\kappa^4)$ term of the spin state's evolution.

Now we return to the damped and dephased spin-oscillator models. In the previous subsection, we showed that the 2-point correlation functions match between the two models, but the 4-point correlation functions do not. Thus, combined with Eqs. (28) and (29), this leads to the conclusion that the spin-state dynamics of the two models agree up to $\mathcal{O}(\kappa^2)$, but not to $\mathcal{O}(\kappa^4)$.

Let $\hat{O}_S(t)$ be a spin observable of interest in the interaction picture. The difference $|\Delta\langle\hat{O}_S(t)\rangle|$ in the expectation value of $\hat{O}_S(t)$ between the damped and dephased spin-oscillator models can be upper bounded using the difference $\Delta C^{(4)}_O(t_0,t_1,t_2,t_3)$ between the 4-point correlation functions in Eqs. (18) and (19). Let $||\cdot||$ denote the max absolute eigenvalue of the argument. By integrating Eq. (29) over time and then applying inequalities such as $|\mathrm{Tr}\{\hat{O}_S(t)\hat{0}\hat{1}\hat{2}\hat{3}\rho'_S(t)\}| \le ||\hat{O}_S|| \times ||\hat{A}_S||^4 = ||\hat{O}_S||/16$, we obtain

$$\begin{aligned}
|\Delta\langle\hat{O}_S(t)\rangle| \le \frac{||\hat{O}_S||}{4}\int_0^t dt_0\int_0^{t_0} dt_1\int_0^{t_1} dt_2\int_0^{t_2} dt_3\Big(|\Delta C^{(4)}_B(t_0,t_1,t_2,t_3)| + |\Delta C^{(4)}_B(t_2,t_0,t_1,t_3)| \\
+|\Delta C^{(4)}_B(t_1,t_0,t_2,t_3)| + |\Delta C^{(4)}_B(t_2,t_1,t_0,t_3)|\Big) + \mathcal{O}(\kappa^6). \qquad (30)
\end{aligned}$$

Note that this upper bound is in similar form to the second-leading order term in Eq. (6) of Ref. [12] (when the exponential is expanded into a Taylor series), which is derived for two spin-boson models with different 2-point correlation functions. For the case of spin-boson models, it is sufficient to consider the difference in only the 2-point correlation functions, as the spin-boson model's bath $\hat{H}_B = \int_0^\infty d\omega\hat{a}^\dagger(\omega)\hat{a}(\omega)$ is Gaussian. However, the *dephased* spin-oscillator model is non-Gaussian; thus, it is necessary to consider the higher-order correlation functions for obtaining such bounds. In practice, for the difference between the damped and dephased spin-oscillator models, the bound in Eq. (30) grows much faster with t than the actual $|\Delta\langle\hat{O}_S(t)\rangle|$ obtained from solving the Lindblad master equations.

IV. RANDOMIZED OPERATIONS

In this section, we explain our method of using randomized control parameters on the quantum harmonic oscillator to (i) prepare the thermal state and (ii) simulate the dephasing. We use the fact that heating and dephasing can be described as an average of many evolutions of closed systems, where the parameter of each closed system's Hamiltonian is randomly drawn [13, 14].

A. Stochastic Lindblad master equation

Consider the stochastic Hamiltonian [14]

$$\hat{H}(t) = \hat{H}_0(t) + \sum_j \lambda_j x_j(t) \hat{L}_j, \tag{31}$$

where $\hat{H}_0(t)$ is the non-stochastic part and

$$\langle x_j(t) \rangle = 0, \quad \langle x_j(t) x_k(t') \rangle = \delta_{jk} \delta(t - t'). \tag{32}$$

Here, $\lambda_j x_j(t)$ represents independent white noise in the strength or phase of the field, where $x_j(t)$ is normalized as in Eq. (32). For convenience, we consider real-valued fields, i.e., λ_j and $x_j(t)$ are real numbers. Then, the density matrix $\rho(t)$, averaged over all realizations of white noise $x_j(t)$, follows the stochastic Lindblad master equation

$$\frac{d\rho(t)}{dt} = -i[\hat{H}_0, \rho(t)] + \sum_j \lambda_j^2 \Big(\hat{L}_j \rho(t) \hat{L}_j^\dagger - \frac{1}{2} \{ \hat{L}_j^\dagger \hat{L}_j,\, \rho(t) \} + \hat{L}_j^\dagger \rho(t) \hat{L}_j - \frac{1}{2} \{ \hat{L}_j \hat{L}_j^\dagger,\, \rho(t) \} \Big). \tag{33}$$

where $\hat{L}_j$ and $\hat{L}_j^\dagger$ turn into Lindblad operators. The proof can be found in Ref. [14]. Note that the strengths assigned to Lindblad operators $\hat{L}_j$ and $\hat{L}_j^\dagger$ are the same.

B. Thermal-state preparation using randomized SDK operations

First, we simulate the infinite-temperature heating, described by a pair of Lindblad operators $\hat{L}_1 = \sqrt{\Gamma'} \hat{b}$ and $\hat{L}_2 = \sqrt{\Gamma'} \hat{b}^\dagger$, by randomizing the motion phase ϕ_m of the SDK operations. The thermal state can be prepared by applying this simulated heating on the motional ground state. The Hamiltonian of the resonant ($\delta_m = 0$) SDK operation with sideband Rabi frequency $\tilde{\Omega}$ and stochastically varying $\phi_m(t)$ is given by

$$\hat{H}(t) = \frac{\tilde{\Omega}}{2} (\hat{b} e^{-i\phi_m(t)} + \hat{b}^\dagger e^{i\phi_m(t)}) = \frac{\tilde{\Omega}}{2} \left(\cos\phi_m(t) (\hat{b} + \hat{b}^\dagger) + \sin\phi_m(t) (-i)(\hat{b} - \hat{b}^\dagger) \right), \tag{34}$$

where $\hat{b}$ here is the annihilation operator of the trapped ions' motional mode. The spin part is ignored as the qubit is prepared in the +1-eigenstate of the SDK Hamiltonian's spin operator.

In practice, we approximate white noise in $\phi_m(t)$ by performing N' discrete steps of SDK operations, where ϕ_m of each step is a constant value randomly drawn from $[0, 2\pi)$. Thus, the values of $\phi_m(t)$ and $\phi_m(t')$ are equal (completely independent) when times t and t' belong to the same (different) discrete step(s). At the limit $\tau' \to 0$, where τ' is the duration of each step,

$$\langle \cos\phi_m(t) \cos\phi_m(t') \rangle = \langle \sin\phi_m(t) \sin\phi_m(t') \rangle \to \frac{\tau'}{4} \delta(t - t'). \tag{35}$$

As $x_1(t)$ and $x_2(t)$ need to be normalized, we plug in $x_1(t) = (2/\sqrt{\tau'}) \cos\phi_m(t)$, $x_2(t) = (2/\sqrt{\tau'}) \sin\phi_m(t)$, $\lambda_1 = \lambda_2 = \tilde{\Omega}\sqrt{\tau'}/4$, $\hat{L}_1 = \hat{b} + \hat{b}^\dagger$, and $\hat{L}_2 = (-i)(\hat{b} - \hat{b}^\dagger)$ into Eq. (31) such that, at the limit $\tau' \to 0$, we obtain the master equation

$$\begin{aligned} \frac{d\rho(t)}{dt} &= \frac{\tilde{\Omega}^2 \tau'}{8} \Big((\hat{b} + \hat{b}^\dagger) \rho(t) (\hat{b} + \hat{b}^\dagger) - \frac{1}{2} \{ (\hat{b} + \hat{b}^\dagger)(\hat{b} + \hat{b}^\dagger),\, \rho(t) \} \\ &\qquad - (\hat{b} - \hat{b}^\dagger) \rho(t) (\hat{b} - \hat{b}^\dagger) + \frac{1}{2} \{ (\hat{b} - \hat{b}^\dagger)(\hat{b} - \hat{b}^\dagger),\, \rho(t) \} \Big) \\ &= \frac{\tilde{\Omega}^2 \tau'}{4} \Big(\hat{b} \rho(t) \hat{b}^\dagger - \frac{1}{2} \{ \hat{b}^\dagger \hat{b},\, \rho(t) \} + \hat{b}^\dagger \rho(t) \hat{b} - \frac{1}{2} \{ \hat{b} \hat{b}^\dagger,\, \rho(t) \} \Big). \end{aligned} \tag{36}$$

This is the Lindblad master equation with Lindblad operators $\hat{L}_1 = \sqrt{\Gamma'} \hat{b}$ and $\hat{L}_2 = \sqrt{\Gamma'} \hat{b}^\dagger$, where

$$\Gamma' = \frac{\tilde{\Omega}^2 \tau'}{4}. \tag{37}$$

The heating strength Γ' is essentially the rate of increase in phonon number over time. Thus, by applying N' steps of these SDK operations on the motional ground state, we prepare the thermal state with average phonon number $\bar{n} = N' \Gamma' \tau' = N' \tilde{\Omega}^2 \tau'^2 / 4$ when averaged over many realizations of random phase $\phi_m(t)$. In our experiments we tune τ' to control $\bar{n}$.

C. Dephased time evolution using randomized SDK operations

Next, we simulate the dephasing during time evolution, described by a single Lindblad operator $\hat{L}_1 = \sqrt{\Gamma}\hat{b}^\dagger\hat{b}$, by adding random offsets to the motion detuning δ_m of the SDK operations. The coherent evolution with respect to $\hat{H}_{SO}$ is simulated using N Trotterization steps, where the SDK operation's duration for each step is τ. Without losing generality, we consider the case where the SDK operations that simulate the coherent evolution use zero motion detuning, such that δ_m denotes the offset ($\nu\hat{b}^\dagger\hat{b}$ term of $\hat{H}_{SO}$ can be simulated by modulating ϕ_m over time, as discussed in the main text). In an appropriate frame, the Hamiltonian of the SDK operation with stochastically varying $\delta_m(t)$ is given by

$$\hat{H}(t) = \hat{H}_0(t) + \delta_m(t)\hat{b}^\dagger\hat{b}, \tag{38}$$

where $\hat{H}_0(t)$ is the part that simulates the coherent evolution.

In our experiments, $\delta_m(t)$ is constant over each Trotterization step, and its value at each step is randomly drawn from a normal distribution $\mathcal{N}(0, \delta_{m,\mathrm{std}})$. Again, the values of $\delta_m(t)$ and $\delta_m(t')$ are equal (completely independent) when times t and t' belong to the same (different) Trotterization step(s). At the limit $\tau \to 0$, we obtain

$$\langle \delta_m(t)\delta_m(t')\rangle \to \frac{\delta_{m,\mathrm{std}}^2\tau}{2}\delta(t-t'). \tag{39}$$

In order to normalize $x_1(t)$, we plug in $x_1(t) = \sqrt{2/\tau}(\delta_m(t)/\delta_{m,\mathrm{std}})$, $\lambda_1 = \sqrt{\tau/2}\delta_{m,\mathrm{std}}$, and $\hat{L}_1 = \hat{b}^\dagger\hat{b}$ into Eq. (31), which gives the master equation

$$\frac{d\rho(t)}{dt} = -i[\hat{H}_0(t), \rho(t)] + \delta_{m,\mathrm{std}}^2\tau\Big(\hat{b}^\dagger\hat{b}\rho(t)\hat{b}^\dagger\hat{b} - \frac{1}{2}\{\hat{b}^\dagger\hat{b}\hat{b}^\dagger\hat{b},\ \rho(t)\}\Big), \tag{40}$$

which is the Lindblad master equation with $\hat{L}_1 = \sqrt{\Gamma}\hat{b}^\dagger\hat{b}$. We set the standard deviation $\delta_{m,\mathrm{std}}$ such that

$$\frac{T}{N\tau}\Gamma = \delta_{m,\mathrm{std}}^2\tau, \tag{41}$$

where the left-hand side is rescaled, as we simulate the evolution up to time T using SDK operations of total duration $N\tau$. This completes our method of simulating the time evolution of the dephased spin-oscillator model.

D. Errors due to finite discretization

As we approximate white noise into discrete steps where randomly drawn parameter is assigned to each step, errors may occur due to finite duration of each step. Here we numerically analyze the errors due to finite discretization.

First, we study the error in thermal-state preparation using randomized operations. In Sec. IV B, we show that SDK operations with random phase simulate infinite-temperature heating, and therefore prepare the thermal state (when starting from the ground state), in the limit $\tau' \to 0$. With a fixed target average phonon number $\bar{n}$ of the thermal state, this limit corresponds to $N' \to \infty$.

We numerically simulate the ensemble of states obtained by many trials of SDK operations with random phase, and plot the fidelity $\mathcal{F}$ between the ensemble and the target thermal state. Figure 5a shows that the thermal state can be prepared with reasonably high fidelity using only a few ($N' < 10$) steps, for the range of $\bar{n}$ considered in this paper. In particular, using 2000 trials and $N' = 9$ discrete steps, the thermal state with $\bar{n} = 2$ can be prepared with error $1 - \mathcal{F} < 10^{-3}$.

For all values of $\bar{n}$, as N' increases from 1, the error decreases at first but then stops decreasing. This shows that in practice, setting N' to a large number may not be effective in preparing a high-fidelity thermal state. Instead, the error floor can be lowered by increasing the number of trials, as shown in Fig. 5a. Also note that for a fixed target fidelity, preparing the thermal state with larger $\bar{n}$ requires more resources (larger N' and/or more trials).

Next, we analyze the error in the rate of dephasing simulated using randomized operations. In Sec. IV C, we show that adding random detunings to the SDK operations is equivalent to dephasing during the time evolution, in the limit $\tau \to 0$, or equivalently, $N \to \infty$.

As in Fig. 2b and e of main text, we numerically simulate the SDK operations with random detuning and fit the population curve to that of the dephased spin-oscillator model, where the dephasing rate Γ is used as the fitting parameter. We choose to use the underdamped cases ($\Gamma = 0.25$ and 0.4), as coherent oscillations give more reliable fitting results. To evaluate the effects of finite N, we plot the errors in the fitted values of Γ for various values of N in Fig. 5b. As expected, the error decreases as N increases.

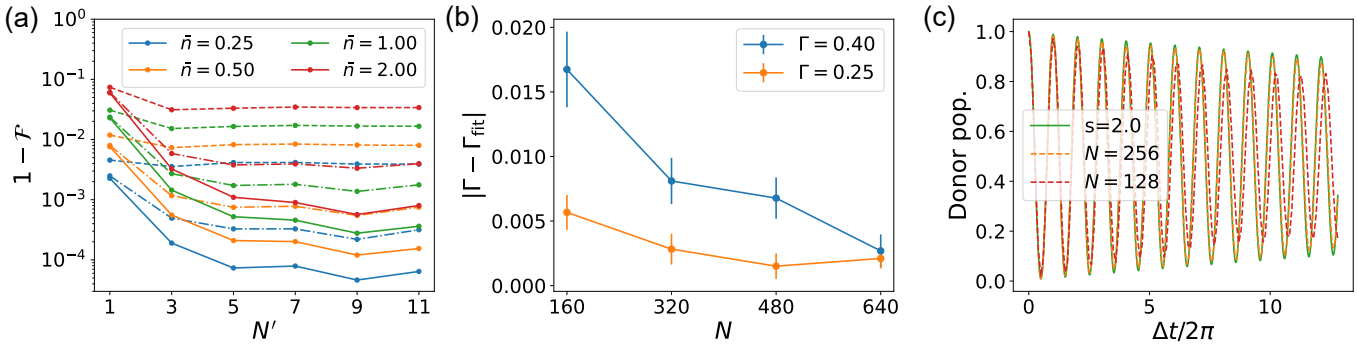

FIG. 5. **Errors due to finite discretization.** **(a)** Errors $1-\mathcal{F}$ in the thermal state prepared using N' steps of SDK operations, where a random phase is assigned to each step. $\mathcal{F}$ is the fidelity between the thermal state of average phonon number $\bar{n}$ and the ensemble of prepared states. The ensemble is obtained by averaging over 20 (dashed), 200 (dot-dashed), and 2000 (solid) trials. For the experimental data in Fig. 2a of main text, we use 20 trials and $N'=5$. **(b)** Errors in the fitted values of Γ, where the population curve obtained by SDK operations is fitted to that of the dephased spin-oscillator model as in Fig. 2e of main text. N is the number of Trotterization steps, each assigned a random detuning. Same Hamiltonian parameters are used as in Fig. 2b of main text. The population curve is averaged over 2000 random trials. Error bars represent the uncertainty of the fitted Γ due to shot noise, where we assume the qubit population is measured only once for each random trial. For the experimental data in Fig. 2b of main text, we use $N=160$, and repeat each of 20 random trials 100 times. **(c)** Simulations of the experiment in Fig. 4d of main text. Green solid curve represents the theoretical predictions of the spin-boson model with spectral density given by the green solid curve in Fig. 4a of main text. Orange (red) dashed curve is the expected results derived from simulating $N=256$ (128) Trotterization steps of SDK operations with random detuning. For the experimental data in Fig. 3d, we use $N=128$, which closely match the red dashed curve as expected.

Note that the error due to finite N discussed here is different from the uncertainty plotted in Fig. 2e of main text, which is due to finite number of random trials. For a larger number (e.g. 2000) of trials, the uncertainty is significantly smaller than the error due to finite N. However, this uncertainty does not take into account shot noise, i.e., uncertainty in qubit population due to finite number of repetitions of binary measurements. For performing a large number of trials, repeating each trial many times to reduce shot noise may require prohibitively long experiment time.

To evaluate the effects of shot noise, we simulate performing 2000 random trials where the qubit state is measured only once for each trial and time step. Specifically, for each random trial, we add a number (0 or 1) randomly drawn from the binomial distribution of success probability p, where p is the simulated qubit population for the corresponding trial and time step. The sum of these numbers over all trials, divided by the number of trials, is the recorded population for each time step. The population curve obtained in this way is fitted as described above. We repeat this entire procedure 100 times and obtain the standard deviation of the fitted Γ values, reported as error bars in Fig. 5b. For $N\leq 480$, the magnitude of this uncertainty due to shot noise is significantly smaller than that of the error in fitted Γ due to finite N. Therefore, higher accuracy in Γ can be achieved with a fixed total number of measurements by performing a larger number of random trials with fewer repetitions. This requires a faster control software that compiles a given set of control parameters [15].

Finally, we discuss the errors due to finite discretization in Fig. 4d of main text. The experimental data obtained using $N=128$ Trotterization steps deviate non-negligibly from the theoretical predictions of the simulated spin-boson model. To explain this mismatch, we numerically simulate performing N SDK operations with random detuning, for $N=128$ and 256. Figure 5c shows that the results for $N=256$ match with the theoretical predictions significantly better than the results for $N=128$. Thus, we expect that the mismatch of our quantum simulation results in Fig. 4d of main text can be removed by using a larger number of Trotterization steps N.

In the experiment, we choose $N=128$ steps owing to the memory constraints of the controlling software. The RF signals utilized for modulating the laser pulses are compiled within a local CPU and stored in the block RAM (BRAM) of a field-programmable gate array (FPGA) board, which has restricted storage capacity for a lengthy instruction of operations. Upgrading both the controlling software and hardware could enable us to perform quantum simulations with a larger number of Trotterization steps.

V. METHODS OF FITTING SPECTRAL DENSITIES

Accurately modeling the dynamics of the spin-boson model requires a reliable representation of the spectral density function $J(\omega)$, which encapsulates the frequency-dependent coupling between the spin and the bosonic environment. In this work, we employ a fitting strategy that approximates the spectral density using a linear combination of basis functions (with some linear constraints, see below), enabling trapped-ion simulations that use finite number of oscillators to simulate a continuum of environment modes. The spectral density to be approximated is from Leggett et al. [16], given by

$$J_{\text{Legg}}(\omega) = A\omega^s \omega_c^{1-s} e^{-\omega/\omega_c}. \tag{42}$$

There are two approaches to fit a spectral density, the spectral density based method and the correlation function based method. The spectral density based method is used to obtain the fitting in the main text. The correlation function based method may serve as an alternative when more flexibility in the fitting parameters is allowed, and we include it here for the readers to better understand the linear constraints used in the spectral density based method.

A. Spectral density based method

The first step in our approach is the discretization of the spectral density function. We utilize the Legendre discretization method [17] to obtain a set of discretized frequencies ω_n and the corresponding weights w_n based on the roots and weights of the Legendre polynomials. The number of grid points N and the frequency domain $[\omega_l, \omega_r]$ ($\omega_l \geqslant 0$ and $\omega_r < \infty$) are chosen to ensure sufficient resolution and coverage of the relevant frequency range. As discussed in the main text, ω_l and ω_r can be chosen to be values such that $[\omega_l, \omega_r]$ cover the range of on-resonance frequencies without detrimenting the correctness of the spin dynamics.

Next, we evaluate the spectral density function $J(\omega)$ at the discretized frequencies ω_n and calculate the coupling strengths V_n^2 as the product of $J(\omega_n)$ and the corresponding weights w_n:

$$V_n^2 = \frac{J_{\text{Legg}}(\omega_n)}{\pi} w_n. \tag{43}$$

These coupling strengths represent the discretized version of the spectral density and serve as the target values for the fitting process.

To approximate the spectral density, we employ a sum of Lorentzian basis functions, which provide a flexible and physically motivated representation [18]. The approximated spectral density function $J_{\text{approx}}(\omega)$ is given by

$$J_{\text{approx}}(\omega) = \sum_{m=1}^{M} J_{\text{Lo},m}(\omega), \tag{44}$$

$$J_{\text{Lo},m}(\omega) = \kappa_m^2 \left(\frac{\Gamma_m/2}{(\Gamma_m/2)^2 + (\omega - \nu_m)^2} - \frac{\Gamma_m/2}{(\Gamma_m/2)^2 + (\omega + \nu_m)^2} \right), \tag{45}$$

where κ_m, γ_m, and ν_m are the parameters of the m-th Lorentzian basis function, representing the coupling strength, damping rate, and peak frequency, respectively. These parameters are optimized during the fitting process to minimize the difference between the target spectral density and the approximating function. As what is done for Leggett's spectral density in Eq. (43), the approximating function $J_{\text{approx}}(\omega)$ is also discretized using the Legendre discretization method, resulting in the same set of frequencies $\{\omega_n\}$ and weights $\{w_n\}$ but different coupling strengths $\tilde{V}_n^2$:

$$\tilde{V}_n^2 = \frac{J_{\text{approx}}(\omega)}{\pi} w_n \tag{46}$$

The optimization is performed by minimizing an objective function defined as the sum of the relative differences between the target and approximated spectral densities at the discretized frequencies:

$$\text{objective} = \sum_{n=1}^{N} \frac{\left| V_n^2 - \tilde{V}_n^2 \right|}{|V_n^2|} \tag{47}$$

We employ Bitmask Evolution Optimization (BITEOPT), a powerful black-box optimization algorithm, to find the optimal values of the Lorentzian parameters. The specific implementation of the algorithm used can be found in Ref. 19.

To ensure physically reasonable values and avoid the deviation of the behaviour of the Lindblad oscillators from the Lorentzian spectral density in Eq. (45), we impose constraints on the Lorentzian parameters during the optimization process. Specifically, we introduce a linear constraint that relates the damping rate γ_m and the peak frequency ν_m of each Lorentzian basis function:

$$\gamma_m \leq \frac{\nu_m}{2}. \tag{48}$$

This constraint is motivated by the condition under which a Lindblad oscillator can be approximated by a Lorentzian spectral density [see the discussion below Eq. (17)]. Additionally, bounds are placed on the parameters to restrict them to physically meaningful ranges, which helps reduce the size of the optimization space. For example, the range of on-resonance frequencies $[\omega_l, \omega_r]$ is set based on the coupling of the spin system. Additionally, the Lorentzian coupling strengths κ_m for each component are restricted to values smaller than the overall system-bath coupling strength.

B. Correlation function based method

Instead of minimizing the discrepancy between spectral densities, we can compare the bath correlation functions (BCF) obtained from the target spectral density (SD-BCF) and the BCF of a Lindblad oscillator (LD-BCF), since the dynamics of the spin in the spin-boson model is solely determined by the BCF [6–8, 20, 21]. The BCFs are calculated using the following expressions [8]

$$C_{\text{SD-BCF}}(t) = \int_0^\infty d\omega \frac{J_{\text{Legg}}(\omega)}{\pi} \left(\frac{\cos\omega t}{\tanh(\beta\omega/2)} - i\sin\omega t \right) \tag{49}$$

$$C_{\text{LD-BCF}}(t) = \kappa^2 e^{-\Gamma t/2} \left(\frac{\cos\nu t}{\tanh(\beta\nu/2)} - i\sin\nu t \right) = \int_0^\infty \frac{\mathrm{d}\omega}{\pi} \left(\frac{\tilde{J}_{\text{Lo}}(\beta,\omega)\cos\omega t}{\tanh(\beta\omega/2)} - iJ_{\text{Lo}}(\omega)\sin\omega t \right) \tag{50}$$

$$J_{\text{Lo}}(\omega) = \kappa^2 \left(\frac{\Gamma/2}{(\Gamma/2)^2 + (\omega-\nu)^2} - \frac{\Gamma/2}{(\Gamma/2)^2 + (\omega+\nu)^2} \right) \tag{51}$$

$$\tilde{J}_{\text{Lo}}(\beta,\omega) = \kappa^2 \frac{\tanh(\beta\omega/2)}{\tanh(\beta\nu/2)} \left(\frac{\Gamma/2}{(\Gamma/2)^2 + (\omega-\nu)^2} - \frac{\Gamma/2}{(\Gamma/2)^2 + (\omega+\nu)^2} \right) \tag{52}$$

where J_{Lo} is the Lorentzian spectral density and $\tilde{J}_{\text{Lo}}$ is the Lorentzian spectral density modified by a factor $\frac{\tanh(\beta\omega/2)}{\tanh(\beta\nu/2)}$.

Fitting the target correlation function $C_{\text{SD-BCF}}(t)$ at a target temperature β by a linear combination of Lindblad oscillators at temperature β_m amounts to matching the real and imaginary parts inside the integral over ω, simultaneously. By allowing the variation of the temperatures of the Lindblad oscillators, we obtain the following two approximation formats, corresponding to the real and imaginary parts of the correlations functions, respectively:

$$\begin{aligned} &\text{Real part:} \quad \frac{J_{\text{Legg}}(\omega)}{\tanh(\beta\omega/2)} \approx \sum_m^M \frac{\tilde{J}_{\text{Lo},m}(\beta_m,\omega)}{\tanh(\beta_m\omega/2)} \Longrightarrow J_{\text{Legg}}(\omega) \approx \sum_m^M \frac{\tanh(\beta\omega/2)}{\tanh(\beta_m\nu/2)} J_{\text{Lo},m}(\omega) \\ &\text{Imaginary part:} \quad J_{\text{Legg}}(\omega) \approx \sum_m^M J_{\text{Lo},m}(\omega). \end{aligned} \tag{53}$$

The two conditions can be fulfilled simultaneously in principle, provided enough flexibility of the parameters β_m, κ_m, Γ_m, ν_m and the number of Lindblad oscillators M. By using the approximations in Eq. (53), we convert the task of fitting the correlation function into a task of fitting the spectral density with two approximations simultaneously. The advantage of the conversion is that, once again, we can specify an on-resonance vibrational frequency range $[\omega_l, \omega_r]$, instead of working on the full frequency range $[\omega_l = 0, \omega_r = \infty]$.

In summary, the proposed two fitting strategies provide a systematic and flexible approach to approximate complex spectral density functions using a linear combination of Lorentzian/Lindblad oscillators. The discretization of the spectral density ensures a tractable computational framework, while the optimization procedure minimizes the discrepancy between the target and approximated functions. The incorporation of physically motivated constraints on the Lorentzian parameters helps to maintain the physical relevance of the fitted spectral density.

VI. LEGGETT'S SPECTRAL DENSITIES WITH FIXED VALUES AT RESONANCE

In Fig. 4 of main text, we simulate Leggett's spin-boson models $J_{\text{Legg}}(\omega) = A\omega^s\omega_c^{1-s}e^{-\omega/\omega_c}$ in the weak spin-bath coupling regime using spectral densities composed of two Lorentzian peaks. As s is increased, the spectral

density value at resonance $J_{\mathrm{Legg}}(\omega = \Delta)$ decreases, and thus the spin-state population's oscillations are damped more weakly. This qualitatively agrees with the analysis of Leggett et al. [16] that the spin dynamics exhibit a transition from localization (extremely strong damping) or incoherent relaxation to coherent oscillations (weak damping) as the exponent s is increased from sub-Ohmic ($s < 1$) to Ohmic ($s = 1$) to super-Ohmic ($s > 1$) values in the strong spin-bath coupling regime. This is consistent with the fact that the spectral density $J_{\mathrm{Legg}}(\omega)$ is scaled with a high cutoff frequency $\omega_c \gg \Delta$, which is an inherent assumption in the model.

Meanwhile, another interesting question is how the spin dynamics behavior of Leggett's model changes when the exponent s is varied under *fixed* spectral density value at resonance $J_{\mathrm{Legg}}(\omega = \Delta)$. While this question deviates significantly from the original physical insights of the Leggett's model, it enables isolating the effects of the spectral density's slope (to first order) while fixing the zero-th order contribution from the resonance value.

Indeed, our method is capable of capturing the difference in the spin dynamics of sub-Ohmic, Ohmic, and super-Ohmic baths even when the resonance value is fixed. Instead of fixing the value of A as in the main text, we consider fixing $J_{\mathrm{Legg}}(\omega = \Delta)$ as s is varied by setting the value of A accordingly ($\omega_c = 10\Delta$ is fixed), and fit the spectral density composed of 3 Lorentzian peaks to $J_{\mathrm{Legg}}(\omega)$ for each s. We find reasonably good fitting results by setting the target bandwidth as $\omega \in [0.5\Delta, 1.5\Delta]$ for the cost function of fitting, which is significantly broader than $[0.9\Delta, 1.1\Delta]$ used in the main text. The target and fitted spectral densities are shown in Fig. 6(a). Note that in this example, the resonant value $J_{\mathrm{Legg}}(\omega = \Delta)$ of the target spectral densities is fixed to 1.57Δ, which is in the relatively strong spin-bath coupling regime.

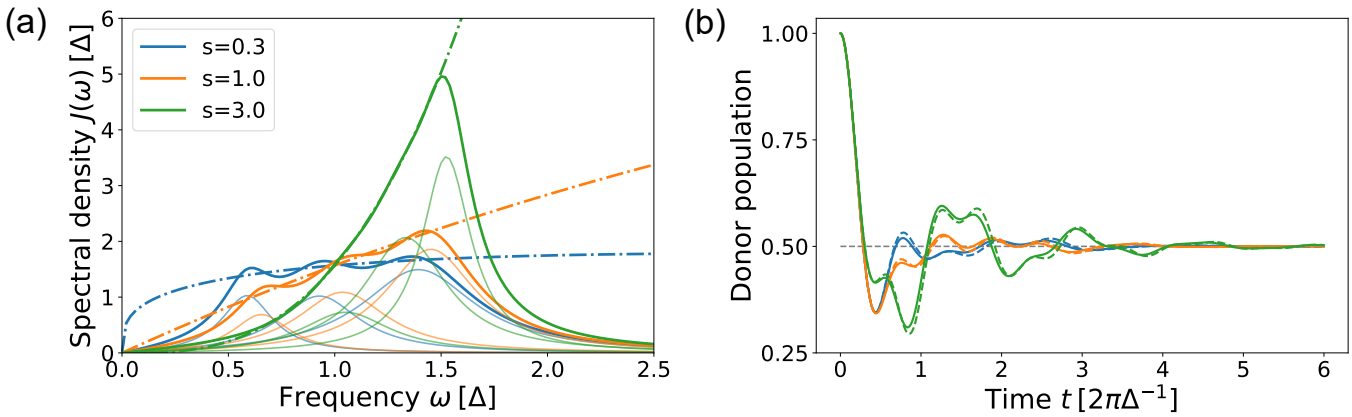

FIG. 6. **Numerical simulations based on Leggett's spectral densities with fixed values at resonance. (a)** $J_{\mathrm{Legg}}(\omega)$ (dash-dotted) and the fitted spectral density consisting of three Lorentzian peaks (solid) for $s = 0.3$, 1, and 3. The constituent Lorentzian peaks are shown in faint solid curves. **(b)** Dynamics of the dephased spin-oscillator models (solid) and the spin-boson models (dashed) with spectral densities given by the solid curves in (a).

Figure 6(b) shows the spin dynamics of the dephased spin-oscillator models and the spin-boson models with the 3-peak spectral densities given in Fig. 6(a). In the super-Ohmic case ($s = 3$), the donor-state population undergoes at least two full oscillations before the population decays to 0.5 (with negligible oscillation amplitude), whereas in the Ohmic ($s = 1$) and sub-Ohmic ($s = 0.3$) cases the population barely undergoes a single oscillation before decaying to near 0.5. This shows that strong coupling to low-frequency bath oscillators induces more rapid population decay than strong coupling to high-frequency bath oscillators, as lower-frequency oscillators are excited to higher phonon-number states and therefore are more strongly subject to dephasing ($\because \hat{a}^\dagger \hat{a} \left|n\right\rangle = n \left|n\right\rangle$) or damping ($\because \hat{a} \left|n\right\rangle = \sqrt{n} \left|n-1\right\rangle$). Also, note that the spin-bath coupling is sufficiently strong for the spin-boson models with different values of s to exhibit different dynamics behavior, yet not too strong such that population dynamics of the spin-boson models do not deviate significantly from those of the dephased spin-oscillator models. Thus, our method of quantum simulations is capable of distinguishing the effects of the exponent s of Leggett's spectral density even when the resonance value is fixed.

Comparing the Ohmic ($s = 1$) and sub-Ohmic ($s = 0.3$) cases, the sub-Ohmic spin-boson model exhibits a faster population decay to near 0.5. This is inconsistent with the simulation results in Fig. 3 of Ref. [22], where the donor-state population decay is significantly faster in the Ohmic case. The analysis of Ref. [22] is different from ours in several ways; (i) the reorganization energy $\int d\omega J(\omega)/\omega$ is fixed among different s values, rather than the resonant $J(\omega = \Delta)$ value, (ii) the spin Hamiltonian consists of four states, and (iii) a stronger spin-bath coupling is considered. Future works may identify in which conditions the population dynamics exhibit "critical damping" (fastest population decay) with the Ohmic spectral density. Quantum simulations using a larger number of oscillators would be able to

cover a wider bandwidth and capture the effects of strong coupling to a broad band of high-frequency oscillators.

[1] A. Chenu and G. D. Scholes, Annual review of physical chemistry **66**, 69 (2015).
[2] Y. Wu, *Quantum Computation in Large Ion Crystals*, Ph.D. thesis, University of Michigan (2019).
[3] Z. Jia, Y. Wang, B. Zhang, J. Whitlow, C. Fang, J. Kim, and K. R. Brown, Physical Review Letters **129**, 103602 (2022).
[4] Z. Jia, *Quantum Information Processing with Spin and Motional States of Trapped Ions*, Ph.D. thesis, Duke University (2022).
[5] H.-P. Breuer and F. Petruccione, *The theory of open quantum systems* (Oxford University Press, New York, USA, 2002).
[6] D. Tamascelli, A. Smirne, S. F. Huelga, and M. B. Plenio, Physical review letters **120**, 030402 (2018).
[7] F. Mascherpa, A. Smirne, A. D. Somoza, P. Fernández-Acebal, S. Donadi, D. Tamascelli, S. F. Huelga, and M. B. Plenio, Phys. Rev. A **101**, 052108 (2020).
[8] A. Lemmer, C. Cormick, D. Tamascelli, T. Schaetz, S. F. Huelga, and M. B. Plenio, New Journal of Physics **20**, 073002 (2018).
[9] H. Grabert, U. Weiss, and P. Talkner, Zeitschrift für Physik B Condensed Matter **55**, 87 (1984).
[10] T. Linowski, A. Teretenkov, and L. Rudnicki, Phys. Rev. A **106**, 052206 (2022).
[11] M. Tokuyama and H. Mori, Progress of Theoretical Physics **55**, 411 (1976).
[12] F. Mascherpa, A. Smirne, S. F. Huelga, and M. B. Plenio, Physical review letters **118**, 100401 (2017).
[13] Z. Cai and T. Barthel, Physical review letters **111**, 150403 (2013).
[14] A. Chenu, M. Beau, J. Cao, and A. del Campo, Physical review letters **118**, 140403 (2017).
[15] A. S. Dalvi, J. Whitlow, M. D'Onofrio, L. Riesebos, T. Chen, S. Phiri, K. R. Brown, and J. M. Baker, arXiv preprint arXiv:2308.10787 (2023).
[16] A. J. Leggett, S. Chakravarty, A. T. Dorsey, M. P. A. Fisher, A. Garg, and W. Zwerger, Rev. Mod. Phys. **59**, 1 (1987).
[17] I. de Vega, U. Schollwöck, and F. A. Wolf, Physical Review B **92**, 155126 (2015).
[18] C. Meier and D. J. Tannor, The Journal of Chemical Physics **111**, 3365 (1999).
[19] D. Wolz, "fcmaes - a python-3 derivative-free optimization library," Available at `https://github.com/dietmarwo/fast-cma-es` (2022), python/C++ source code, with description and examples.
[20] A. D. Somoza, O. Marty, J. Lim, S. F. Huelga, and M. B. Plenio, Phys. Rev. Lett. **123**, 100502 (2019).
[21] D. Tamascelli, A. Smirne, J. Lim, S. F. Huelga, and M. B. Plenio, Physical review letters **123**, 090402 (2019).
[22] N.-N. Zhang, M.-J. Tao, W.-T. He, X.-Y. Chen, X.-Y. Kong, F.-G. Deng, N. Lambert, and Q. Ai, Frontiers of Physics **16**, 1 (2021).